Multiparametric optimization of the middle vanes of a counter-rotating axial impulse turbine for Oscillating Water Column devices

A. Vega-Valladares, M. Garcia-Diaz, B. Pereiras, and M. Takao

Abstract—**Oscillating Water Column devices have been historically one of the most studied Wave Energy Converters. Despite the existence of other alternatives, bidirectional turbines are the most widespread solution to take advantage of the characteristic bidirectional air flows in these devices. This category mainly includes Wells and impulse turbines. M. E. McCormick introduced the counter-rotating impulse turbines in 1978. Unlike the aforementioned, these specific impulse turbines mount two counter-rotating rotors. Thus, the downstream rotor is able to harness the kinetic energy at the output of the upstream rotor. These turbines traditionally achieved poor efficiencies at low flow rates due to the misalignment of the flow between rotors. More recently, the introduction of a row of Middle Vanes between the two rotors was proposed in order to overcome this drawback. In this work, a CFD-based optimization of the Middle Vanes of a counter-rotating axial impulse turbine is presented. The Mixing Plane technique was used to simulate the relative movement of the blades. Three geometric parameters used to define the shape of the Middle Vanes, as well as the number of them, were considered as Input Parameters for the optimization. Meanwhile, the total-to-static efficiency reached by the turbine at a flow coefficient of 1 was set as the only Output Parameter to maximize in this multiparametric and single-objective optimization, this leading to a 1.2% improvement in terms of peak efficiency.**

Keywords—**CFD, Counter-rotating impulse turbines, optimization, OWC, WECs.**

I. INTRODUCTION

AMONG the different Wave Energy Converters (WECs), Oscillating Water Column (OWC) devices have been the most popular for decades [1]. As shown in Fig. 1, an OWC device consists of three parts: an OWC chamber, a Power Take Off (PTO), which is normally an air turbine, and a generator. The chamber is open at the bottom to the sea and at the top to the atmosphere. The incoming and outgoing waves produce an oscillatory up and down movement of the water column inside the chamber, which in turn generates a bidirectional airflow in and out of that chamber. Thus, the pneumatic energy is converted into mechanical energy by the air turbine which finally drives the generator to produce electricity.

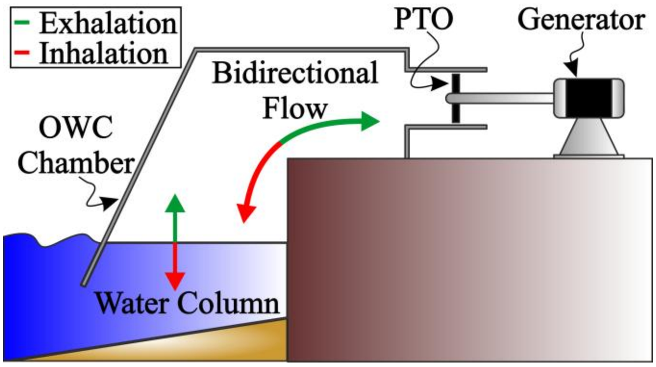

Fig. 1. Principle of operation of an OWC device.

Bidirectional turbines, also known as self-rectifying turbines, represent the most common solution to take advantage of the two classical operating stages in these OWC devices: exhalation and inhalation (see Fig. 1) [2]. Wells and impulse turbines have been historically the most famous bidirectional turbines [3]. However, both of them present some associated drawbacks. Wells turbines were patented by A. A. Wells in 1976 [4]. They can achieve higher peak efficiencies than the impulse turbines, but they present a narrow range of operating flow rates. Meanwhile, impulse turbines were patented by I. A. Babintsev in 1975 [5], representing the main alternative to the Wells turbines. They present a wider range of flow rates, but their peak efficiencies are normally lower than those achieved by the Wells turbines.

Part of a special issue for EWTEC 2025. Original version published in EWTEC 2025 proceedings at doi.org/10.36688/ewtec-2025-857.

A. Vega-Valladares is supported by the "Administración del Principado de Asturias" within the "Severo Ochoa" Program under grant number BP21-160. This work was also supported by the project PID2024-160067OB-I00, funded by the Spanish Ministry of Science, Innovation and Universities.

A. Vega-Valladares, M. Garcia-Diaz and B. Pereiras are with the University of Oviedo, Energy Department, C/ Wifredo Ricart s/n, 33204 Gijón, Spain (e-mail: vegaaitor@uniovi.es, garciadmanuel@uniovi.es, pereirasbruno@uniovi.es).

M. Takao is with the Matsue College, National Institute of Technology, Mechanical Engineering Department, Nishiikuma-cho, 14-4, 690-8518 Matsue, Japan (e-mail: takao@matsue-ct.jp).

Digital Object Identifier: https://doi.org/10.36688/imej.9.83-90

On the other hand, M. E. McCormick, from the United States Naval Academy, introduced the counter-rotating impulse turbines for wave energy conversion in 1978 [6]. As shown on the left side of Fig. 2, unlike those aforementioned, this specific type of impulse turbines incorporates two counter-rotating rotors. In this way, the downstream rotor is able to harness the kinetic energy at the output of the upstream rotor.

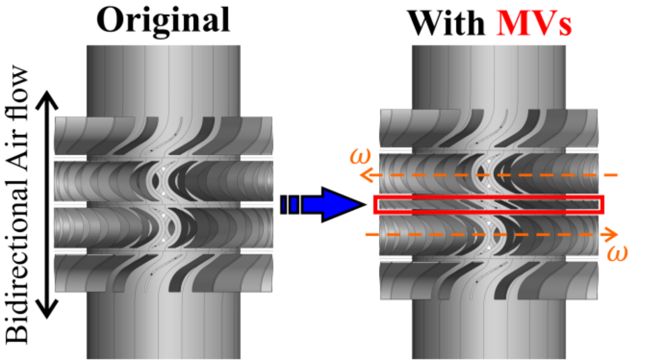

Fig. 2. Counter-rotating axial impulse turbine: original version (left) and incorporating a row of Middle Vanes (right).

Nevertheless, these counter-rotating impulse turbines also present some disadvantages, such as the noise and the complexity of their shaft, the latter contributing to the increase of the manufacturing costs. Apart from that, the first experimental tests, which were performed by D. Richards et al. in 1986, reported a poor average efficiency of about 30% for these counter-rotating impulse turbines [7]. However, not enough data about the performance of these turbines could be found in the literature, so Manabu Takao et al. carried out further research, proving through CFD analysis that these counter-rotating impulse turbines, at high flow rates, achieved higher efficiencies than the traditional impulse turbines incorporating a single rotor [8]. But the main problem was that, at low flow rates, these turbines achieved lower efficiencies than those incorporating a single rotor due to the flow misalignment produced between the two counter-rotating rotors [9]. Thus, as could be seen on the right side of Fig. 2, Manabu Takao et al. proposed the introduction of a row of Middle Vanes (MVs) between the two counter-rotating rotors in order to overcome the above problem [10]. Several CFD studies carried out in recent years have proven the efficiency improvement achieved by these counter-rotating impulse turbines, especially at low flow rates, thanks to the presence of this additional row of MVs [11], [12]. Thus, encouraged by the promising numerical results obtained so far, Manabu Takao et al. built an experimental model, and those efficiency improvements were finally confirmed through experimental tests, these results coming to light precisely at the last edition of the European Wave and Tidal Energy Conference (EWTEC), which was held in 2023 in Bilbao, Spain [13].

In this work, a CFD-based optimization of the MVs of a counter-rotating axial impulse turbine is presented. Three geometric parameters used to define the shape of these MVs, as well as the number of them, were taken as the four Input Parameters (IPs) for the optimization process. Meanwhile, the Output Parameter (OP) of this multiparametric and single-objective optimization was the total-to-static efficiency achieved by the turbine at a flow coefficient of 1. Obviously, the objective function consisted of maximizing this OP. The results show a total-to-static peak efficiency improvement of approximately 1.2%. Thus, the promising results obtained in this work encourage the authors to continue improving the optimization process in order to allow this counter-rotating axial impulse turbines to achieve even higher efficiencies.

II. MATHEMATICAL FORMULATION

The performance of the turbine of an OWC device is traditionally assessed through the following dimensionless coefficients: flow coefficient (ϕ), torque coefficient (C_T), input coefficient (C_A) and total-to-static efficiency ($\eta_{t\text{-}s}$).

These dimensionless coefficients are defined as follows:

$$\phi = \frac{v}{u} \tag{1}$$

$$C_T = \frac{2T_o}{\rho(v^2 + u^2)AR_m} \tag{2}$$

$$C_A = \frac{2\Delta P_{t-s}}{\rho(v^2 + u^2)} \tag{3}$$

$$\eta_{t-s} = \frac{\omega T_o}{\Delta \mathrm{P}_{t-s} Q} \tag{4}$$

Where ρ is the air density, T_o is the output torque of the turbine, $\Delta P_{t\text{-}s}$ is the total-to-static pressure drop in the turbine, Q is the flow rate, ω is the rotational speed, R_m is the mean radius of the turbine, u is the tangential velocity at the mean radius of the turbine, A is the crossflow area of the turbine, and v is the axial velocity. Note that the output torque of the turbine is the sum of the mechanical torque provided by the upstream rotor (T_{o_usr}) and by the downstream rotor (T_{o_dsr}). Meanwhile, the same rotational speed was set for the two counter-rotating rotors.

In addition, note that the total-to-static efficiency can be also expressed in terms of the other dimensionless coefficients as follows:

$$\eta_{t-s} = \frac{C_T}{C_A \phi} \tag{5}$$

Furthermore, as shown in Fig. 3, the turbine geometry has been divided into five different parts: inlet + upstream

GVs, upstream rotor, MVs, downstream rotor and downstream GVs + outlet. Note that the terms *upstream* and *downstream* are used to denote those parts of the turbine located upstream and downstream of the MVs, respectively, the MVs obviously being bounded by sections C and D in this Fig.3.

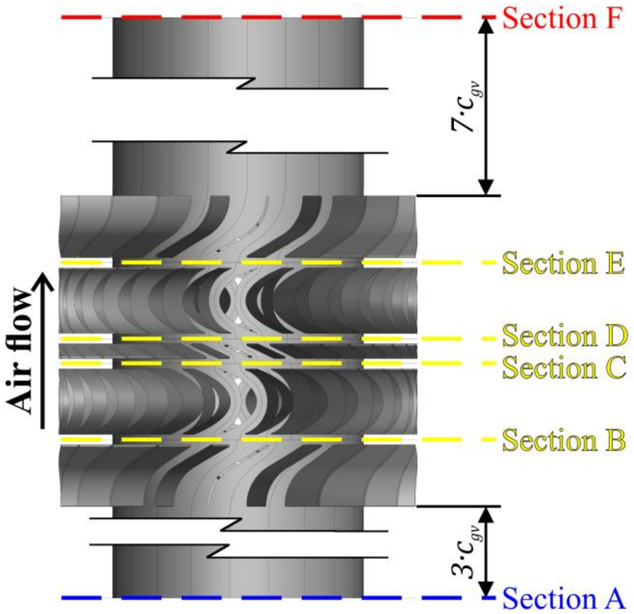

Fig. 3. Turbine sections considered for the rotor efficiencies.

Thus, the efficiency of the upstream rotor (η_{usr}) and the efficiency of the downstream rotor (η_{dsr}), which are also used in this work to assess the performance of the turbines, are calculated considering the total-to-total pressure drops ($\Delta P_{t\text{-}t}$) between the corresponding sections shown in Fig. 3 as follows:

$$\eta_{usr} = \frac{\omega T_{o\_usr}}{\Delta P_{t-t}^{B-C} Q} \tag{6}$$

$$\eta_{dsr} = \frac{\omega T_{o\_dsr}}{\Delta P_{t-t}^{D-E} Q} \tag{7}$$

III. GEOMETRY

The turbine geometry was created in the commercial software ANSYS DesignModeler v23.2. The base case geometry of the counter-rotating axial impulse turbine analyzed in this work was taken from [13]. The size of the turbine was not modified in this work. Hence, the original hub radius (R_{hub}) and shroud radius (R_{shr}) of the turbine were kept constant during the optimization process, taking a value of 84 and 120 mm, respectively. Thus, the mean radius of the turbine (R_m) takes a value of 102 mm. Apart from that, as can be appreciated in Fig. 4, a null tip clearance was considered for all turbine rows in this work, so the blade span of the rotor blades, MVs and GVs (b) takes a value of 36 mm.

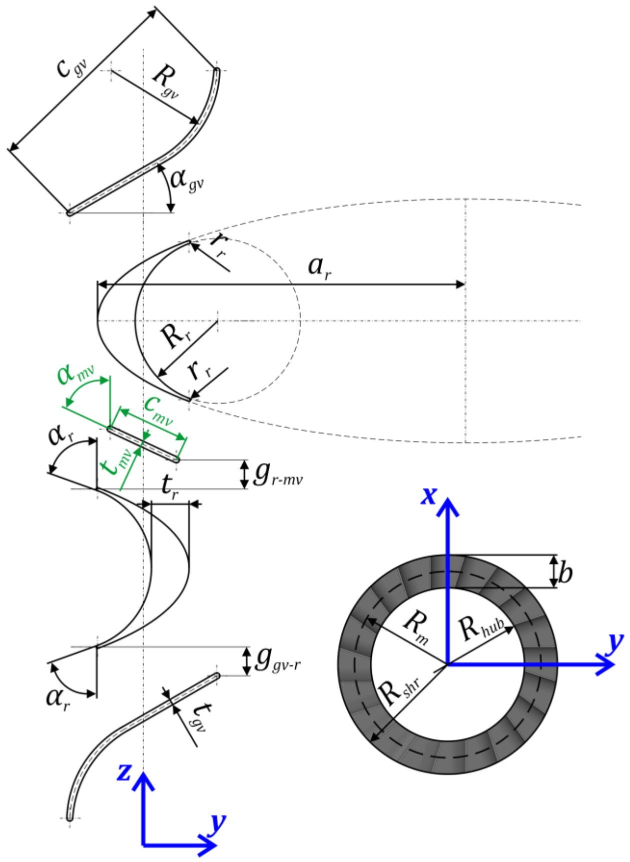

Fig. 4. Geometric parameters of the turbine.

As can be observed in Fig. 4, the MVs consist of thin flat plates. The three geometric parameters necessary to define the shape of those MVs and taken as IPs for the optimization process are shown in green in this Fig. 4. The value taken by those IPs, as well as by the other parameters necessary to define the shape of the rotor blades and GVs of the turbine, are collected in Table I.

TABLE I
VALUE OF THE BASE CASE GEOMETRY PARAMETERS

Turbine row	Parameter	Unit	Value
GVs	c_{gv}	mm	56
	R_{gv}	mm	29.8-
	t_{gv}	mm	1.6
	Z_{gv}	-	20
	α_{gv}	°	30
GVs to Rotor	$g_{gv\text{-}r}$	mm	8
Rotor	a_r	mm	100.6
	r_r	mm	0.4
	R_r	mm	22.586
	t_r	mm	10.3
	Z_r	-	30
	α_r	°	70
Rotor to MVs	$g_{r\text{-}mv}$	mm	8
MVs	c_{mv}	mm	20
	t_{mv}	mm	1.6
	Z_{mv}	-	34
	α_{mv}	°	65

In addition, the gap distance between GVs and rotors ($g_{gv\text{-}r}$) and between rotors and MVs ($g_{r\text{-}mv}$), as well as the number of elements that compound each turbine row, can be also consulted in Table I. Remember that the number of

MVs (Z_{mv}) was taken as the fourth IP for the optimization process. Nevertheless, the number of GVs (Z_{gv}) and the number of rotor blades (Z_r) were kept constant in this work.

IV. MESH AND NUMERICAL MODEL

Structured meshes of around 450k hexahedral cells were generated in the commercial software ANSYS TurboGrid v23.2 to carry out the simulations during the optimization process. This mesh size was enough to guarantee relative errors below 1% for those variables involved in the calculation of the OP if the results obtained with a much finer mesh of around 3.6M cells are taken as a reference. However, once the optimization process was completed, meshes with around 900k cells were used to simulate the whole performance curves associated with both the base case geometry and the optimized one over a wider range of flow coefficients. Note that this higher mesh density was adopted, not for the purpose of achieving more accurate results, but to be able to visualize the flow patterns inside the turbine with a higher resolution when analyzing those results in more depth. In addition, not only a sensitivity analysis of the mesh size was carried out in this work, but also a grid analysis in terms of quality was performed following the minimum angle criterion. 64% of the cells are in the range between 81° and 90°, which represents an excellent orthogonality of the mesh and ensures enough quality for CFD proposals. In fact, the minimum internal angle reached in any of the mesh cells takes a value of 44.34°, which is indeed quite a high value [14].

The simulations were carried out by using the commercial solver ANSYS Fluent v23.2. The different computational domain volumes and boundary conditions (BCs) implemented for the numerical model are shown in Fig. 5. The whole computational domain was divided into five different volumes corresponding to the five parts of the turbine bounded by those sections shown in Fig. 3. In order to save computational resources, only one channel of the turbine was simulated taking advantage of the typical periodic BCs following the contour of the vanes and blades. Nevertheless, note that the number of elements of each turbine row was different (see Table I). Hence, the Mixing Plane technique was adopted to simulate the relative movement of the rotor blades in order to allow each of the computational domain volumes to comprise a different angle of the whole turbine. The same rotational speed (*ω=500 rpm*) was set for the two counter-rotating rotors. Accordingly, several set of interfaces were introduced to allow the use of nonconformal grids between the different static and moving volumes. Nonslip walls were considered for the GVs, rotor blades, MVs, hub and shroud of the turbine. A pair of velocity-inlet/pressure-outlet BCs were introduced at the inlet and outlet of the computational domain, respectively. Atmospheric conditions were always considered at the outlet. Meanwhile, the velocity at the inlet took a fixed value corresponding to a flow coefficient of 1 when simulating each of the Design Points (DPs) during the optimization process, but it was modified in each simulation carried out latter to obtain the whole performance curves of the turbines over a wider range of flow coefficients.

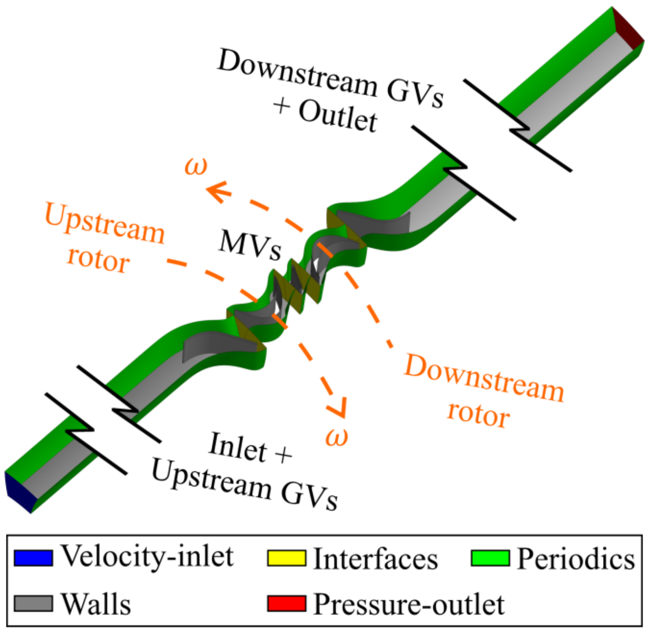

Fig. 5. Computational domain volumes and Boundary Conditions (shroud wall suppressed).

For the turbulence modelling, the k-ε Realizable model was chosen taking into account its well-known robustness and ability to work in low-speed turbomachinery environments [14]. In addition, the Enhanced Wall Treatment was also adopted, taking special care that the values taken by the y+ parameter were below 1 in the proximity of all the domain walls. Indeed, 69.38% of the cells in the domain walls satisfy this condition, and 98.37% of them take y^+ values below 2. Apart from that, the pressure-velocity coupling was recreated through the Coupled algorithm, and other relevant parameters of the spatial discretization are contained in Table II.

TABLE II
SPATIAL DISCRETIZATION PARAMETERS

Parameter	Value
Gradient	Least Squares Cell Based
Pressure	Second Order
Momentum	Third-Order MUSCL
Turbulent Kinetic Energy	Third-Order MUSCL
Turbulent Dissipation Rate	Third-Order MUSCL

Finally, the simulations were carried out on a computer equipped with an Intel i7-5820K processor with 6 cores and 32 GB of DDR4 RAM memory. With the residuals set to a low enough value of 10^{-6} to ensure the convergence, 2000 iterations were needed to complete the simulation of each DP during the optimization process, taking approximately 55 minutes to simulate each DP and generate the geometry associated with the following DP. Meanwhile, 2000 iterations were needed to complete each of the simulations necessary to obtain the whole performance curves of the turbines, taking in this case around 2 hours and 40 minutes to simulate each flow coefficient with the mesh of 900k cells.

V. OPTIMIZATION PROCESS

The geometry, mesh and solver blocks were all integrated in ANSYS Workbench v23.2 and automatically updated for the simulation of each DP during the optimization process, which was carried out by using the ANSYS DesignXplorer v23.2 optimization tools package. In particular, the search for the optimum value of the IPs considered in this work was based on the use of Response Surfaces (RSs). The point of using RSs is the ability to predict the value that the OPs would take for a given combination of IPs but without the need to really run the simulation. In this specific type of optimization processes, first of all, it is necessary to complete a Design of Experiments (DoE). Thus, a determined number of initial DPs are simulated, with the IPs taking different values properly distributed within the Design Space (DS) assessed. Then, the RSs are generated for the first time by using the numerical results obtained for those initial DPs associated with the DoE. However, unless the number of IPs and their allowed variation limits are small enough, additional Refinement Points (RPs) will be necessary in order to improve the accuracy of the RSs. Logically, these two aspects are decisive in the computational times needed to complete the optimization processes. Finally, once the accuracy of the RSs is high enough, an optimization algorithm is used to predict the optimum combination of IPs.

The number of MVs (Z_{mv}), as well as the three geometric parameters shown in green in Fig. 4: MVs chord (c_{mv}), MVs thickness (t_{mv}) and MVs setting angle (α_{mv}), were the four IPs considered for the optimization process presented in this work. Note that the three geometric parameters necessary to define the shape of the MVs were treated as continuous IPs, being possible for them to take any value between their Lower Limit (LL) and Upper Limit (UL) of variation during the optimization process. Meanwhile, the number of MVs was treated as a discrete IP, and five levels of variation were contemplated during the optimization process: 28, 31, 34, 37 and 40. Note that a greater resolution for this discrete parameter would be unnecessary, since a variation of one or two MVs would not have a significant effect on the turbine performance but would significantly increase the time required to complete the optimization process. Table III, where the magnitude of the DS can be easily appreciated, contains the LL and UL set for the four IPs considered in this work. In addition, the percentage of variation allowed for each IP with respect to their initial value is shown in brackets in this Table III. On the other hand, the base case geometry taken from [13] reached the total-to-static peak efficiency at a flow coefficient of 1. In this vein, the total-to-static efficiency achieved by the turbine at that flow coefficient of 1 was considered as the only OP for the optimization process presented in this work.

TABLE III
INPUT PARAMETERS: LOWER LIMITS, INITIAL VALUES AND UPPER LIMITS

IP	Unit	LL (%)	Initial Value	UL (%)
c_{mv}	mm	17 (15%)	20	25 (25%)
t_{mv}	mm	0.48 (70%)	1.6	1.84 (15%)
Z_{mv}	-	28 (17.6%)	34	40 (17.6%)
α_{mv}	°	55.25 (15%)	65	74.75 (15%)

On this occasion, the DoE was performed by using the typical Central Composite Design (CCD) method in its enhanced face-centered version. 146 initial DPs were simulated to complete this DoE, and 304 additional RPs were necessary to improve the accuracy of the RSs, which were generated by Genetic Aggregation (GA). Finally, the search for the optimum combination of IPs was carried out by the use of a single-objective algorithm with the ability to handle discrete parameters, the Mixed-Integer Sequential Quadratic Programming (MISQP) algorithm, since maximizing the OP was the only goal here. In addition, the optimization algorithm was programmed to propose three different candidates, thus ensuring the full exploration of the DS and minimizing the risk of identifying a false optimum geometry after finding a local maximum of the OP within that DS. Table IV shows the predicted and simulated values of the OP for the base case geometry and for the three candidates. Note that a negligible relative error (ε) below 0.1% is always shown in the last column of this Table IV, which proves the high accuracy of the RSs. Candidate 1, which offers the best performance, was finally selected by the authors as the optimized geometry.

TABLE IV
OUTPUT PARAMETERS: PREDICTED VALUES, SIMULATED VALUES AND RELATIVE ERRORS

Geometry	OP	Unit	Predicted	Simulated	ε (%)
Base case	$\eta_{t\text{-}s}$	-	0.51764	0.51740	0.04639
Candidate 1	$\eta_{t\text{-}s}$	-	0.52963	0.52965	0.00378
Candidate 2	$\eta_{t\text{-}s}$	-	0.52921	0.52927	0.01134
Candidate 3	$\eta_{t\text{-}s}$	-	0.52918	0.52952	0.06421

As can be seen in Table V, the three IPs used to define the shape of the MVs have experienced a significant variation, but without reaching the LL nor the UL in any case. However, the optimized geometry incorporates the same number of MVs than the base case geometry. Focusing on Candidate 1, two out of four IPs have increased. The MVs chord has experienced a remarkable increase of 13.14% with respect to its initial value. Meanwhile, the MVs setting angle has experienced a less significant increase of 6.05%. On the other hand, the MVs thickness has decreased greatly, by 64.88%. This phenomenon was expected by the authors, since Manabu Takao et al. had concluded in previous studies that low t_{mv}/c_{mv} ratios were beneficial for the performance of this type of counter-rotating axial impulse turbines [12].

Bearing this in mind, the authors of the present work decided to set a wider UL and a wider LL for the MVs chord and for the MVs thickness, respectively (see Table III). Nevertheless, note that, according to [12], a MVs thickness value lower than the LL shown in Table III for this IP would have been unfeasible if the optimized geometry was experimentally tested.

TABLE V
INPUT PARAMETERS: OPTIMUM VALUES OF THE THREE CANDIDATES

IP	Unit	Candidate 1	Candidate 2	Candidate 3
c_{mv}	mm	22.628	21.098	20.660
t_{mv}	mm	0.562	0.553	0.550
Z_{mv}	-	34	34	34
α_{mv}	°	68.932	69.117	69.186

In Fig. 6, it can be observed how the shape of the MVs has changed after the optimization process carried out in this work. It can be clearly appreciated how the optimized MVs are now longer and thinner than in the base case geometry taken from [13], in addition to being more inclined if the axial direction is taken as a reference.

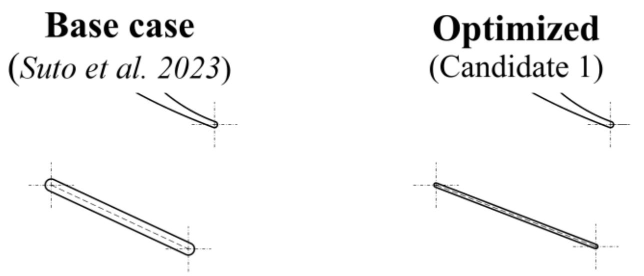

Fig. 6. Comparison between the base case geometry taken from [13] (left) and the optimized geometry Candidate 1 (right).

VI. RESULTS AND DISCUSSION

The numerical results obtained in the simulations for the base case geometry and for the optimized geometry (Candidate 1) are analyzed and compared in this section over a wider range of flow coefficients.

The torque coefficients offered by the upstream rotor (C_{T_usr}) and by the downstream rotor (C_{T_dsr}) are respectively shown in Fig. 7 (a) and Fig. 7 (b) for both geometries. On the one hand, as can be observed in Fig. 7 (a), the torque coefficients offered by the upstream rotor are practically identical for both geometries, since nothing has really changed in the turbine geometry upstream of the MVs. On the other hand, as can be observed in Fig. 7 (b), the torque coefficients offered by the downstream rotor of the optimized geometry are clearly higher than those offered by the downstream rotor of the base case geometry over the entire range of flow coefficients.

The results discussed above are reflected in the efficiencies achieved by the upstream and downstream rotors, which are respectively shown in Fig. 8 (a) and Fig. 8 (b) for both geometries. On the one hand, as can be observed in Fig. 8 (a), the efficiencies achieved by the upstream rotor are practically identical for both geometries, similar to what could be appreciated before in Fig. 7 (a) when talking about torque coefficients. On the other hand, as can be observed in Fig. 8 (b), the efficiencies achieved by the downstream rotor of the optimized geometry are remarkably higher than those achieved by the downstream rotor of the base case geometry over the entire range of flow coefficients, which could be explained by the also higher torque coefficients that could be appreciated before in Fig. 7 (b). A remarkable improvement of 4.93% has been achieved in terms of peak efficiency. While the downstream rotor of the base case geometry reached a peak efficiency of 79.82% at a flow coefficient of 1.25, the downstream rotor of the optimized geometry reaches a peak efficiency of 84.75% at a flow coefficient of 0.75.

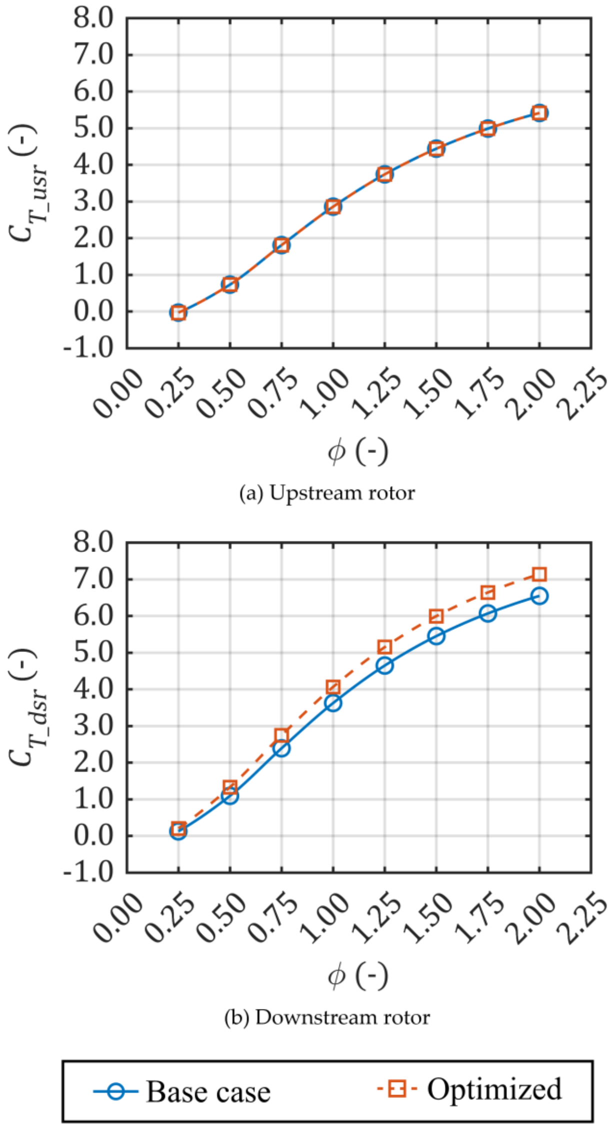

Fig. 7. Performance comparison in terms of torque coefficient offered by: (a) Upstream rotor and (b) Downstream rotor.

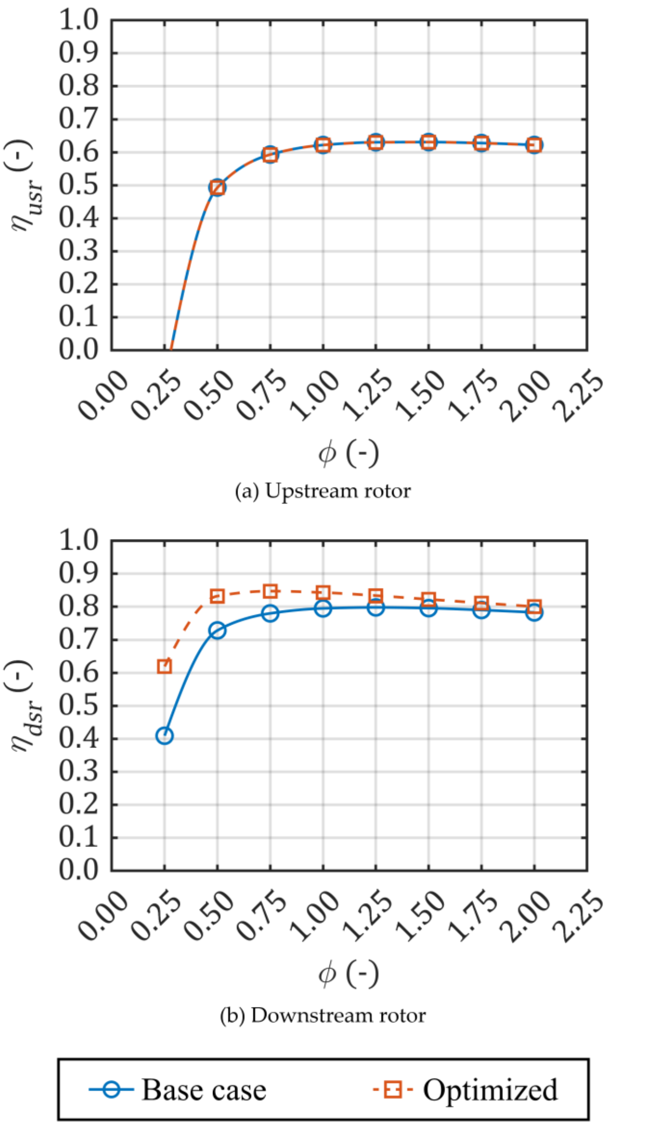

(a) Upstream rotor

(b) Downstream rotor

Fig. 8. Performance comparison in terms of rotor efficiencies achieved by: (a) Upstream rotor and (b) Downstream rotor.

The evolution of the torque and input coefficients of the whole turbine are respectively shown in Fig. 9 (a) and Fig. 9 (b) for both geometries. Remember that the torque coefficients shown in Fig. 9 (a) correspond to the sum of the torque coefficients shown in Fig. 7 (a) and Fig. 7 (b) for the two counter-rotating rotors of the turbines individually. According to (5), an increase in torque coefficients and a decrease in input coefficients would lead to the improvement of the total-to-static efficiencies achieved by the turbine. As can be observed in Fig. 9 (b), the input coefficients reached by the optimized geometry are higher than those reached by the base case geometry over the entire range of flow coefficients due to the higher value taken by the MVs setting angle, which leads to a major blockage of the flow. Nevertheless, as can be observed in Fig. 9 (a), the torque coefficients reached by the optimized geometry are also higher than those reached by the base case geometry due to the higher torque coefficients offered by the downstream rotor of the turbine after the MVs optimization, thanks to the better guidance of the flow between the two counter-rotating rotors. In the end, as can be observed in Fig. 9 (c), this increase in torque coefficients outweighs the increase in input coefficients, so that the total-to-static efficiencies achieved by the optimized geometry turn out to be higher than those achieved by the base case geometry over the entire range of flow coefficients.

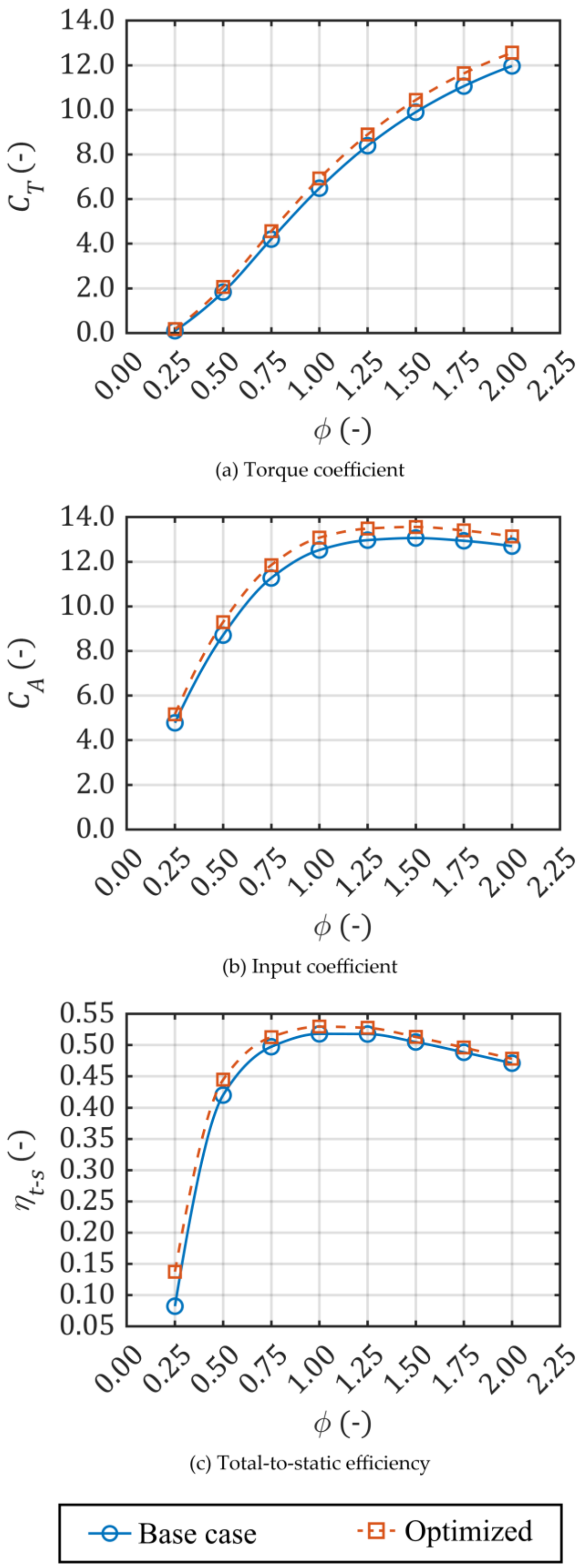

(a) Torque coefficient

(b) Input coefficient

(c) Total-to-static efficiency

Fig. 9. Performance comparison in terms of: (a) Torque coefficient, (b) Input coefficient and (c) Total-to-static efficiency.

As can be appreciated in Fig. 9 (c), the total-to-static peak efficiency reached by the counter-rotating axial impulse turbine analyzed in this work has been improved by 1.16%. While the base case geometry reached a total-to-static peak efficiency of 51.81% at a flow coefficient of 1, the optimized geometry reaches a peak efficiency of 52.97% at the same flow coefficient. Even more significant improvements of up to 5.53% have been achieved at lower flow coefficients.

VII. Conclusions

A CFD-based optimization of the Middle Vanes (MVs) of a counter-rotating axial impulse turbine is presented in this work.

The MVs were simple thin flat plates. Three geometric parameters used to define the shape of the MVs, as well as the number of them, were taken as the four Input Parameters (IPs) considered for the optimization process. Meanwhile, the total-to-static efficiency achieved by the turbine at a flow coefficient of 1 was the only Output Parameter (OP) in this multiparametric and single-objective optimization, the objective function obviously consisting of maximizing this OP.

The simulations were carried out on ANSYS Fluent v23.2 by the use of the Mixing Plane technique, and the optimization process was entirely performed within the ANSYS Workbench v23.2 environment by the use of the ANSYS DesignXplorer v23.2 optimization tools package. The results revealed approximately a 1.2% improvement in terms of total-to-static peak efficiency, this motivated by the better performance of the downstream rotor after the MVs optimization. A remarkable improvement of around 4.9% has been achieved in terms of the peak efficiency reached by the downstream rotor of the turbine.

In view of the promising results obtained in this work, the authors are encouraged to enhance the optimization process in order to further improve the efficiencies achieved by these counter-rotating axial impulse turbines. Geometric parameters necessary to define the shape not only of the MVs, but also of the Guide Vanes (GVs) and the rotor blades of the turbine, will be included as IPs in the following works of the authors in order to carry out a much more complete optimization before testing the optimized geometry experimentally.

References

[1] A. F. de O. Falcão, "Wave energy utilization: A review of the technologies," *Renewable and Sustainable Energy Reviews*, vol. 14, no. 3, pp. 899–918, 2010, doi: 10.1016/j.rser.2009.11.003.

[2] A. F. O. Falcão and J. C. C. Henriques, "Oscillating-water-column wave energy converters and air turbines: A review," *Renew Energy*, vol. 85, pp. 1391–1424, 2016, doi: 10.1016/j.renene.2015.07.086.

[3] T. Setoguchi and M. Takao, "Current status of self rectifying air turbines for wave energy conversion," *Energy Convers Manag*, vol. 47, no. 15–16, pp. 2382–2396, Sep. 2006, doi: 10.1016/j.enconman.2005.11.013.

[4] A. A. Wells, "Fluid driven rotary transducer, British Patent Spec. No. 1595700," 1976

[5] I. A. Babintsev, "Apparatus for Converting Sea Wave Energy Into Electrical Energy, Patent no US 3922739," 1975

[6] M. E. McCormick, *Ocean wave energy conversion*. in Alternate energy. New York: Wiley, 1981.

[7] D. Richards and F. B. Weiskopf, "Studies With, and Testing of the McCormick Pneumatic Wave Energy Turbine With Some Comments on PWECS Systems," *Coastal Engineering*, pp. 80–102, 1987.

[8] M. Takao, K. Yamada, M. M. A. Alam, S. Okuhara, and T. Setoguchi, "Performance Analysis of Counter-Rotating Impulse Turbine for Wave Energy Conversion," *Turbomachinery*, vol. 45, no. 4, pp. 222–228, 2017, doi: 10.11458/tsj.45.4_222.

[9] M. Takao, K. Yamada, S. Okuhara, M. M. A. Alam, Y. Kinoue, and T. Setoguchi, "A Counter-Rotating Impulse Turbine for Wave Energy Conversion," *Open Journal of Fluid Dynamics*, vol. 08, no. 04, pp. 435–442, 2018, doi: 10.4236/ojfd.2018.84028.

[10] M. Takao, K. Yamada, M. M. Ashraful Alam, S. Okuhara, Y. Kinoue, and S. Nagata, "Counter-rotating impulse turbine for wave energy conversion — Performance improvement by means of middle vane," in *2017 IEEE 6th International Conference on Renewable Energy Research and Applications (ICRERA)*, 2017, pp. 111–114. doi: 10.1109/ICRERA.2017.8191250.

[11] M. Takao, K. Yamada, R. Sasaki, M. M. A. Alam, S. Okuhara, and Y. Kinoue, "A study of counter-rotating impulse turbine for wave energy conversion - Effect of middle vane on the performance," in *IOP Conference Series: Earth and Environmental Science*, Institute of Physics Publishing, Mar. 2019. doi: 10.1088/1755-1315/240/5/052001.

[12] T. Ogawa, M. Takao, M. M. A. Alam, S. Okuhara, and Y. Kinoue, "A study of counter-rotating impulse turbine for wave energy conversion-effect of middle vane thickness on the performance," in *Journal of Physics: Conference Series*, Institute of Physics, May 2022. doi: 10.1088/1742-6596/2217/1/012073.

[13] K. Suto *et al.*, "Experimental Investigation on Performance of Counter-rotating Impulse Turbine with Middle Vanes for Wave Energy Conversion," in *Proceedings of the European Wave and Tidal Energy Conference*, European Wave and Tidal Energy Conference, Sep. 2023. doi: 10.36688/ewtec-2023-451.

[14] A. Vega-Valladares, M. Garcia-Diaz, and B. Pereiras, "Multi-objective response surface optimization of a centrifugal turbine for application in oscillating water column devices equipped with a twin turbine configuration," *Ocean Engineering*, vol. 324, Apr. 2025, doi: 10.1016/j.oceaneng.2025.120629.